Aragonite is calcite's best friend at the seafloor

Olivier Sulpis (o.j.t.sulpis@uu.nl)
Utrecht University https://orcid.org/0000-0002-6463-3320
Priyanka Agrawal
Utrecht University
Mariette Wolthers
Utrecht University
Guy Munhoven
Université de Liège
Matthew Walker
University of Lincoln https://orcid.org/0000-0002-9865-1375
Jack Middelburg
Utrecht University https://orcid.org/0000-0003-3601-9072

Article

Keywords: aragonite, calcite, seafloor

Posted Date: September 22nd, 2021

DOI: https://doi.org/10.21203/rs.3.rs-776722/v1

Version of Record: A version of this preprint was published at Nature Communications on March 1st, 2022. See the published version at https://doi.org/10.1038/s41467-022-28711-z.

Aragonite is calcite's best friend at the seafloor

Olivier Sulpis[1], Priyanka Agrawal[1], Mariette Wolthers[1], Guy Munhoven[2], Matthew Walker[3], Jack J. Middelburg[1]

[1]Department of Earth Sciences, Utrecht University, The Netherlands

[2]Département d'Astrophysique, Géophysique et Océanographie, Université de Liège, Belgium

[3]School of Life Sciences, University of Lincoln, United Kingdom

Corresponding author: Olivier Sulpis (o.j.t.sulpis@uu.nl)

Abstract

In the open ocean, calcium carbonates are mainly found in two mineral forms. Calcite, the least soluble, is widespread at the seafloor, while aragonite, the more soluble, is rarely preserved in marine sediments. Despite its greater solubility, research has shown that aragonite, which could contribute between 10 and 90% to pelagic calcium carbonate production, is able to reach the deep-ocean. If large quantities of aragonite settle and dissolve at the seafloor, this represents a large source of alkalinity that buffers the deep ocean and favours the preservation of less soluble calcite, acting as a deep-sea, carbonate version of galvanization. Here, we investigate the role of aragonite dissolution on the early diagenesis of calcite-rich sediments using a novel 3D, micrometric-scale reactive-transport model combined with 3D, X-ray tomography structures of natural aragonite and calcite shells. Results highlight the important role of diffusive transport in benthic calcium carbonate dissolution, in agreement with recent work. We show that, locally, aragonite fluxes to the seafloor could be sufficient to suppress calcite dissolution in the top layer of the seabed, possibly causing calcite recrystallization. As aragonite producers are particularly vulnerable to ocean acidification, the proposed galvanizing effect of aragonite could be weakened in the future, indirectly boosting calcite dissolution further.

Introduction

More than a quarter of the Earth's surface is covered by marine sediments rich in calcium carbonate ($CaCO_3$),[1,2] whose dissolution represents the ultimate natural sink for anthropogenic carbon dioxide (CO_2).[3] In the open ocean, most $CaCO_3$ originates from the near surface[4,5], where it is secreted by organisms as building blocks of their shells and skeletons in diverse crystalline structures. Calcite is the most stable $CaCO_3$ mineral under Earth surface conditions[6], and it is believed that calcite accounts for the majority of the oceanic $CaCO_3$ reservoir[7]. Thus, in the majority of existing biogeochemical models used to predict and reconstruct Earth climates[8-11], all $CaCO_3$ is treated as the mineral calcite. There is, however, growing evidence that aragonite, another $CaCO_3$ mineral more soluble than pure calcite[6], could account for a large part of, and even dominate $CaCO_3$ production and cycling[12-15].

In the open ocean, aragonite production is dominated by shelled pteropods and heteropods, abundant free swimming sea snails[12,14], and to a lesser extent, by some foraminifera[16] and cold-water coral species[17]. Upon the organisms death, aragonite shells settle through the water column, where they start to dissolve[18] due to internal organic matter degradation[19], to their increasing solubility with increasing hydrostatic pressure[20] and to the buildup of metabolic CO_2 in deep

waters[21]. The remaining aragonite deposits at the seafloor. Below the aragonite saturation depth, the depth at which seawater undersaturation with respect to aragonite first occurs and below which aragonite should dissolve, aragonite grains are rarely preserved in sediments[22]. This largely contrasts with calcite, which is commonly found in marine sediments up to several kilometers below the calcite saturation depth[2,23]. That aragonite disappears shallower than calcite in sediments is coherent with aragonite's greater solubility, but why is aragonite not preserved in sediments below its saturation horizon whilst calcite ordinarily is? Potential reasons include the presence of calcite dissolution inhibitors in sediments, or fast aragonite dissolution kinetics, but both are still uncertain or unsupported by recent laboratory experiments[24,25].

Although rarely preserved in sediments, there is clear evidence that aragonite reaches the seafloor even deep below its saturation depth. Sediment traps have recorded high concentrations of pteropod genetic material[26] and suspended aragonite[24] far below the aragonite saturation depth. Thus, a large proportion of settling aragonite grains in the ocean could dissolve at or near the sediment-water interface. Let us now consider a sedimentary system in which calcite and aragonite are both present in seawater undersaturated with respect to both minerals, i.e., surrogate for a deep-sea sediment. From a thermodynamic perspective, aragonite and calcite should both dissolve, releasing alkalinity and raising $CaCO_3$ saturation states (Ω). Since aragonite is more soluble than calcite, if aragonite dissolution is fast enough, then as long as aragonite is present and dissolving, seawater could remain oversaturated with respect to calcite. As there is nothing to keep seawater saturated with respect to aragonite, since it is the most soluble mineral present, aragonite would eventually fully dissolve. In this picture, the interaction between calcite and aragonite is unidirectional, and the preferential preservation of calcite in sediments is caused by the dissolution of deposited aragonite at the seafloor. This represents a deep-sea, carbonate version of galvanization, in which aragonite sacrifies itself to protect the underlying calcite.

Observing aragonite dissolution at the seafloor in situ is difficult because of the limited spatial and temporal resolution of instruments able to reach the deep ocean. Using existing sediment-porewater models is also an imperfect approach, because these models mathematically express grains (e.g., shells) as a spatial continuum of solid[27-29] rather than three-dimensional entities with microstructures and heterogeneities. Thus, existing models are unable to resolve chemical gradients within a single pore, or across the surface of a single grain. Here, we use a novel three-dimensional model, to simulate dissolution reactions at the micrometer scale for a variety of natural $CaCO_3$ grains virtually placed in seawater (Fig. S1), within which chemical reactions, their rates, and transport processes were resolved. The model equations, assumptions, initial conditions and boundary conditions for each simulation are described in the *Materials and Methods*. We demonstrate that molecular diffusion generates large disparities in dissolution rates across mineral surfaces within a single $CaCO_3$ shell, which may account for part of the disagreement among published empirical $CaCO_3$ dissolution rate laws. Then, we simulate the dissolution of an aragonite pteropod shell sitting on top of a calcite sediment bed in a typical deep-sea setting, and show that aragonite dissolution indeed exerts a galvanizing action by favouring the preservation of surrounding calcite particles.

Results and discussion

Heterogeneous dissolution of $CaCO_3$ shells

Most experimental assessments of $CaCO_3$ dissolution rates in seawater to date have measured bulk dissolution rates, by computing dissolution rates from a mass or water-chemistry change over a given amount of time[30-33]. This approach yields the overall dissolution rate, including transport processes, rather than the rate of true dissolution at the mineral surface[34,35]. In particular, molecular diffusion could lead to a buildup of dissolution products next to the mineral surface, which could locally buffer seawater and raise $CaCO_3$ saturation states[36].

In volumes of undersaturated seawater, we virtually dissolve a set of foraminifera and pteropod e-specimens obtained from X-ray tomography scans (see *Materials and Methods*) and present micrometer-scale resolution visualizations of $CaCO_3$ saturation states and dissolution rates (Fig. 1). In each simulation, after only one minute, water inside the dissolving shells is at or near equilibrium with respect to the dissolving $CaCO_3$ phase (Fig. 1a-d). At this point, dissolution essentially only occurs on the external faces of the shells (Fig. 1e-h). The distributions of calcite dissolution rates across the foraminifera shell surfaces appear bimodal (Fig. S2): internal faces display dissolution rates approaching zero, while external faces dissolve with rates ranging between 1.5 and 4 $\times 10^{-7}$ mol m^{-2} s^{-1}. Aragonite dissolution patterns are similar. External faces of the pteropod shell dissolve at rates between 4 and 5.5 mol m^{-2} s^{-1} while internal faces do not, as they are in contact with seawater at or close to equilibrium with respect to aragonite. This very wide range of values is in line with the range of calcite and aragonite dissolution rates measured in the laboratory, in seawater with a similar bulk chemical composition (Fig. S3). Thus, part of the reason why the variability in measured dissolution rates is so large across experiments could be because solute transport, the rate-limiting step in overall dissolution, is specific to each sample and experimental design. When expressing the overall dissolution rate of a $CaCO_3$ grain, its mass, rather than its surface area, may be a better property of normalization.

The specific surface areas of the foraminifera and pteropod e-specimens used in these simulations, i.e., their surface area per mass unit, are one to two orders of magnitude smaller than specific surface areas measured from the same species using the Kr-BET method[24,31,37,38]. The spatial resolution of our e-specimens is possibly not high enough to capture submicroscale features such as surface roughness and shell microporosity. Since our model underestimates mineral surfaces available for reactions, it also likely underestimates how quickly equilibrium can be reached within dissolving shells and minimizes local transport limitations. In our simulation conditions and in the absence of water advection, only the external faces of $CaCO_3$ shells should dissolve, as the inner parts will be at or close to equilibrium. In the following, we therefore replace calcite foraminifera shells by calcite spheres (Table S2) of similar diameter for simplicity.

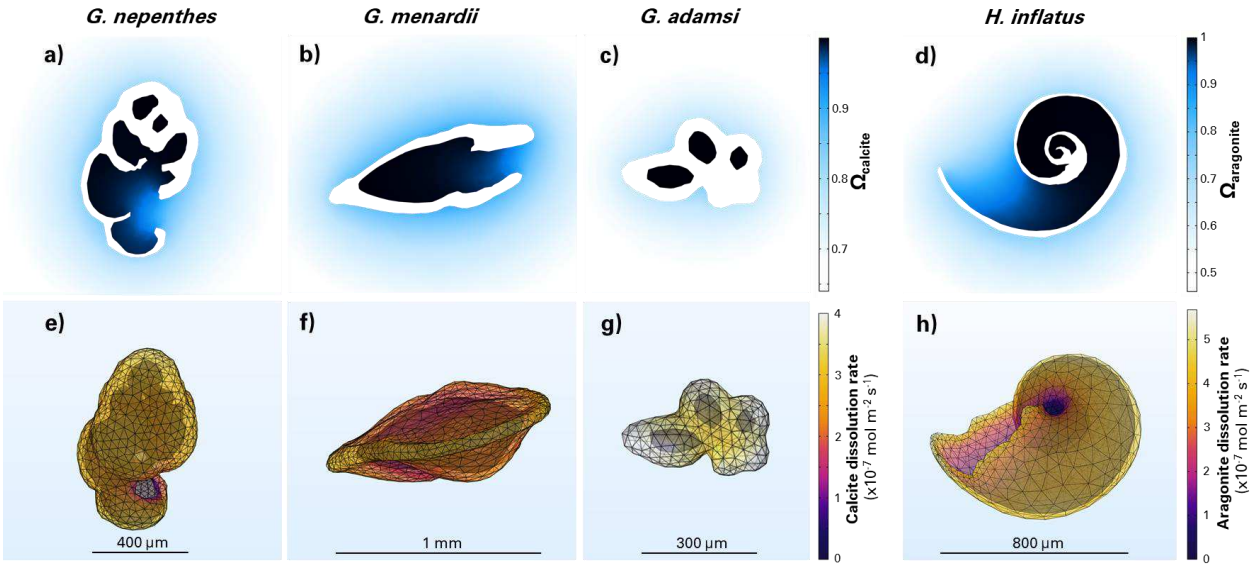

Figure 1. Dissolution of natural marine $CaCO_3$ grains after a minute in suspension in water. The top row shows the water saturation state of calcite (a,b,c) and aragonite (d) while on the bottom row the corresponding calcite (e,f,g) and aragonite (h) dissolution rates are displayed.

Pteropod shell dissolution at the seafloor

Upon death, pteropods settle rapidly and therefore spend only a few hours or days in the water column[39]. Once at the seafloor, due to very slow accumulation rates of typical deep-sea sediments (a few centimeters per thousand years), pteropods should spend a much greater time at or just below the sediment-water interface (a few decades or centuries, unnacounting for bioturbation and dissolution) and, thus, play a role in early diagenesis of surrounding particles. We simulate the dissolution of an empty pteropod shell placed on a calcite sediment bed overlain by seawater undersaturated with respect to both calcite and aragonite ($\Omega_{calcite}$ ~ 0.64, $\Omega_{aragonite}$ ~ 0.46, Table S1). Each calcite particle in this sediment is a sphere with a 150 µm-radius, surrogate for a typical foraminifera. The sediment bed is overlain by a 1.5-mm thick diffusive boundary layer (Fig. S1), within which solutes are transport via molecular diffusion. These conditions are typical of deep-sea benthic environments[23]. The dissolution simulations were run for 5 minutes, until a steady state was reached.

In a pure-calcite sediment bed, porewaters reach equilibrium with respect to calcite a few hundred µm below the sediment-water interface (Fig. 2) and most of the $\Omega_{calcite}$ gradient is within the diffusive boundary layer rather than the sediment (Fig. 2). This is in agreement with results from previous modeling[40,41] and laboratory[35] works on calcite-rich sediments depleted of organic-matter and aragonite. In this classical setting, the chemical gradients should be laterally homogeneous, and lead to an efflux of dissolution products from the sediment toward the bottom waters. The top layer of calcite grains should dissolve until another layer settles in, and the fraction of the calcite grains that escaped dissolution is buried, eventually, and preserved in the sediment record.

Using the same framework but replacing four calcite spheres at the sediment-water interface by an aragonitic pteropod (Fig. S1), chemical gradients appear much different (Fig. 2). In this simulation, only ~6% of the sediment-water (horizontal) interface surface area (3.15 mm × 3.15 mm ≈ 10 mm^2, see *Materials and Methods*) is aragonite, the rest is calcite (32%) and water (62%). In the depth transect across the dissolving pteropod, water $\Omega_{calcite}$ increases from ~0.64 at the top of the diffusive boundary layer to ~1.3 at about 200 μm below the sediment-water interface, before decreasing again deeper in the porewaters and converging toward equilibrium (Fig. 2). Horizontally averaging $\Omega_{calcite}$ over the entire sediment mesh, we find that porewaters are saturated with respect to calcite all the way up to the sediment-water interface due to the presence of the dissolving pteropod shell (Fig. S4). In this setting, dissolution products diffuse from the pteropod shell upward to the bottom waters, but also downward and sideways, and a halo of calcite supersaturation develops in the porewaters beneath the dissolving aragonite (Fig. 2). This causes the calcite grains surrounding the pteropod to be partially in contact with supersaturated water, thermodynamically preventing their dissolution, despite the bottom waters overlaying this sediment being strongly undersaturated with respect to calcite. Over the entire resolved domain, calcite grains sitting at the sediment-water interface only dissolve on their upper half (Fig. 3) with dissolution rates always lower than those from single-foraminifera simulations (Fig. 1,3).

The predicted seawater calcite supersaturation that surrounds dissolving aragonite particles at the seafloor could account for some of the calcite recrystallization occasionally observed on the surface of preserved foraminifera[42,43]. This mechanism could thus require to reconsider the contribution of authigenic $CaCO_3$ formation to the total $CaCO_3$ burial rate in sediments, thought to be ~10%[44] and mainly due to deeper diagenetic processes such as bacterial sulfate reduction[44,45].

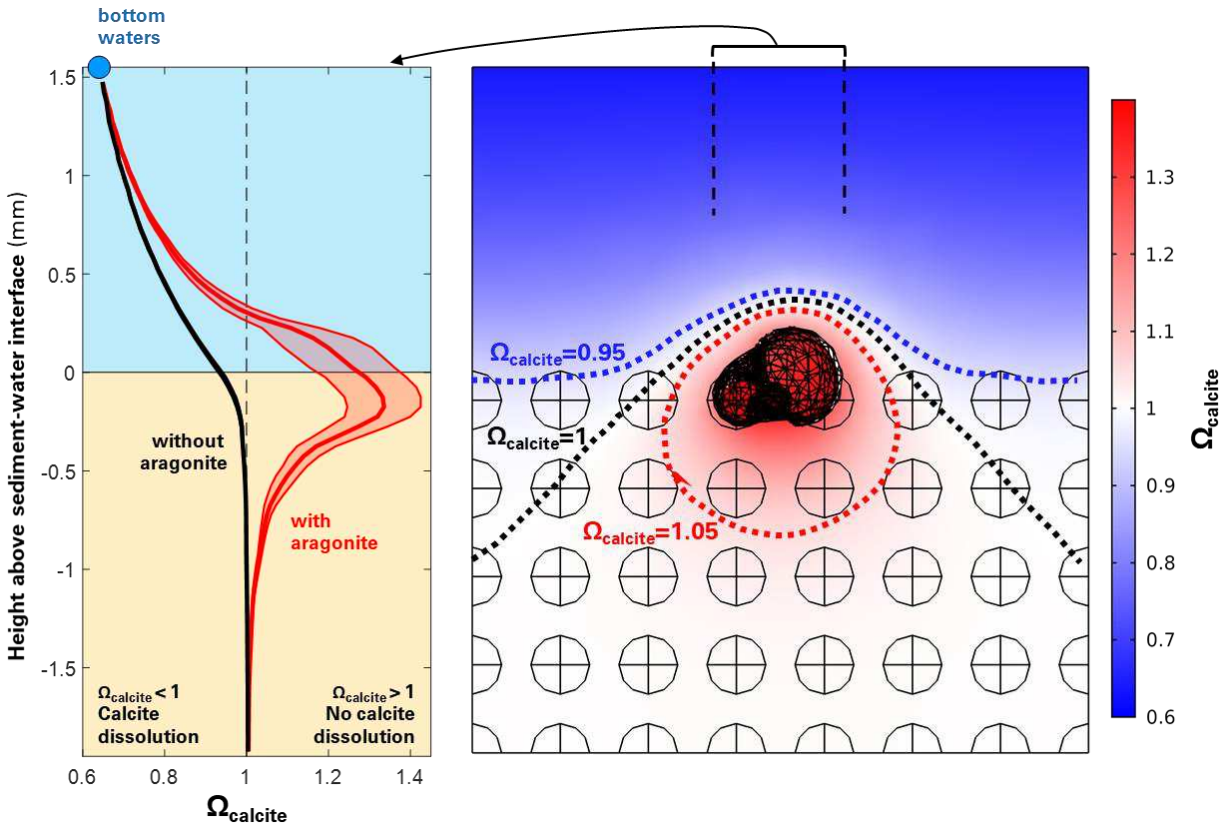

Figure 2. Effects of the dissolution of a pteropod shell on the saturation state with respect to calcite across the sediment-water interface. (Left) Depth profile of the saturation state with respect to calcite. The blue circle represents the bottom-water value. The black depth profile stands for a case without aragonite, the red depth profile represents the situation with aragonite shown on the right. Each depth profile is computed as the mean amongst all data points within the central 850µm×850µm column, which corresponds to the size of the pteropod shell, plus and minus one standard deviation. The extent of the colored enveloped surrounding the mean profiles stands for the standard deviation. (Right) Depth transect of water saturation state with respect to calcite, with contours for three selected saturation state values.

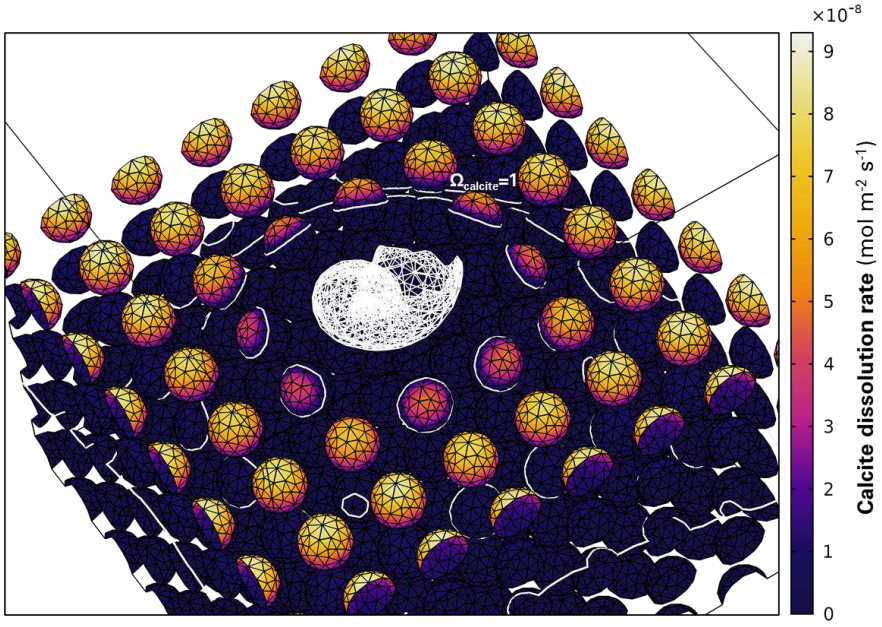

Figure 3. Dissolution of calcite grains in a sediment bed capped with a dissolving aragonite pteropod. The pteropod is shown in a white mesh. Colour gradients indicate surface calcite dissolution rates. The white lining represents a saturation state with respect to calcite of unity, i.e., a transition from undersaturation to supersaturation with respect to calcite that is caused by the dissolving aragonite pteropod.

Implications for $CaCO_3$ cycling

Aragonite can only play a meaningful role in calcite benthic dynamics via its galvanizing action if the aragonite flux to and the residence time at the seafloor are high enough. Unfortunately, little is known about the sources and sinks of aragonite in the ocean. For instance, published estimates of the contribution of pteropod aragonite to global $CaCO_3$ production in the modern ocean span a very wide range from ~10% to ~90%[13,14,46]; this does not account for aragonite produced by heteropods and benthics organisms. In addition, the spatial distribution of aragonite production and export is unknown, although it is thought that pteropods are most abundant in high-latitude systems[47]. At the seafloor, the world-averaged $CaCO_3$ deposition rate is estimated to range between 0.08 and 0.14 mol m^{-2} a^{-1},[7] and we cannot exclude the possibility that a substantial fraction of that amount is deposited in the form of aragonite.

It would take about twice as long for a pteropod to dissolve at the seafloor than when falling through the water column (Fig. 4). The preferential preservation of pteropods at the sediment-water interface is due to the strong transport limitation dictated by molecular diffusion within sediment porewaters and the diffusive boundary layer above the bed, and to the presence of dissolving calcite spheres beneath it. It takes ~200 days to fully dissolve an ~800 µg aragonite sphere (Table S2) at the seafloor (Fig. 4). A ~60 µg pteropod shell (Table S2) should, by extrapolation, fully dissolve in ~15 days. Given that one pteropod shell is able to maintain ~10 mm^2 of calcite seafloor (super)saturated with respect to calcite all the way up to the sediment-water interface (Fig. S4), at least one new pteropod shell needs to be delivered every 15 days, every 10 mm^2 of seafloor in order to sustain galvanization by aragonite. Using 60 µg as a typical pteropod shell weight, this translates into an aragonite deposition rate of ~0.14 mol m^{-2} a^{-1}, on the higher end of the world-averaged total $CaCO_3$ deposition rate to the seafloor. Thus, it is likely that, locally, calcite particles are preferentially preserved due to aragonite dissolution at the seafloor.

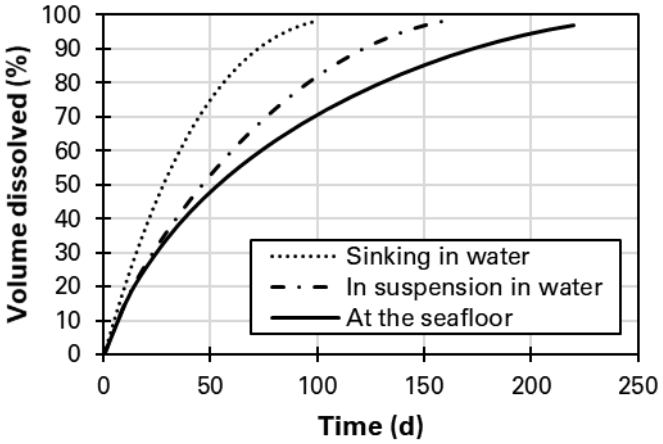

Figure 4. Dissolution of aragonite spheres as a function of time. The simulations did not run until full dissolution because of the increasing difficulty to produce a mesh for dissolving particles as they become smaller. The dotted line represents dissolution for an aragonite sphere sinking through water, the dash/dot line stands for dissolution of a particle in suspension in water, and the solid line is the case for an aragonite sphere sitting above a calcite-spheres sediment.

Diagenetic processes excluded from the present abiotic model could affect the results presented here in various ways. One the one hand, microbial degradation of organic matter that releases CO_2 and drives additional $CaCO_3$ dissolution[19,48,49] should reduce the residence time of pteropod shells and other aragonite grains at the seafloor, thus hindering their galvanizing action. On the other hand, biological mixing caused by bioturbating organisms should transport aragonite grains from the sediment-water interface to depth, favouring aragonite preservation and disseminating aragonite "buffering pills" within the sediment. More broadly, our results highlight the need for future model-, field- and laboratory-based studies about marine $CaCO_3$ dynamics to consider the presence of several carbonate minerals simultaneously, with different compositions and structures, as they not only passively coexist but chemically interact with each other.

Materials and methods

Model

All simulations were performed in COMSOL Multiphysics®, using the PARDISO solver and a Backward-Euler time stepping method. Eight dissolved species (H^+, OH^-, $H_2CO_3^*$, HCO_3^-, CO_3^{2-}, Ca^{2+}, Na^+, Cl^-) and 2 solid species (calcite, aragonite) were included. For each dissolved species, initial concentrations were determined using the PHREEQC software[50] at 25°C, for a water density of 1023.6 kg m^{-3} and a total alkalinity of 1950 µmol kg^{-1}, so that the resulting saturation state of water with respect to calcite ($\Omega_{calcite}$) was about 0.64, a value typical of the deep sea (Table S1; Dunne, et al. [51]).

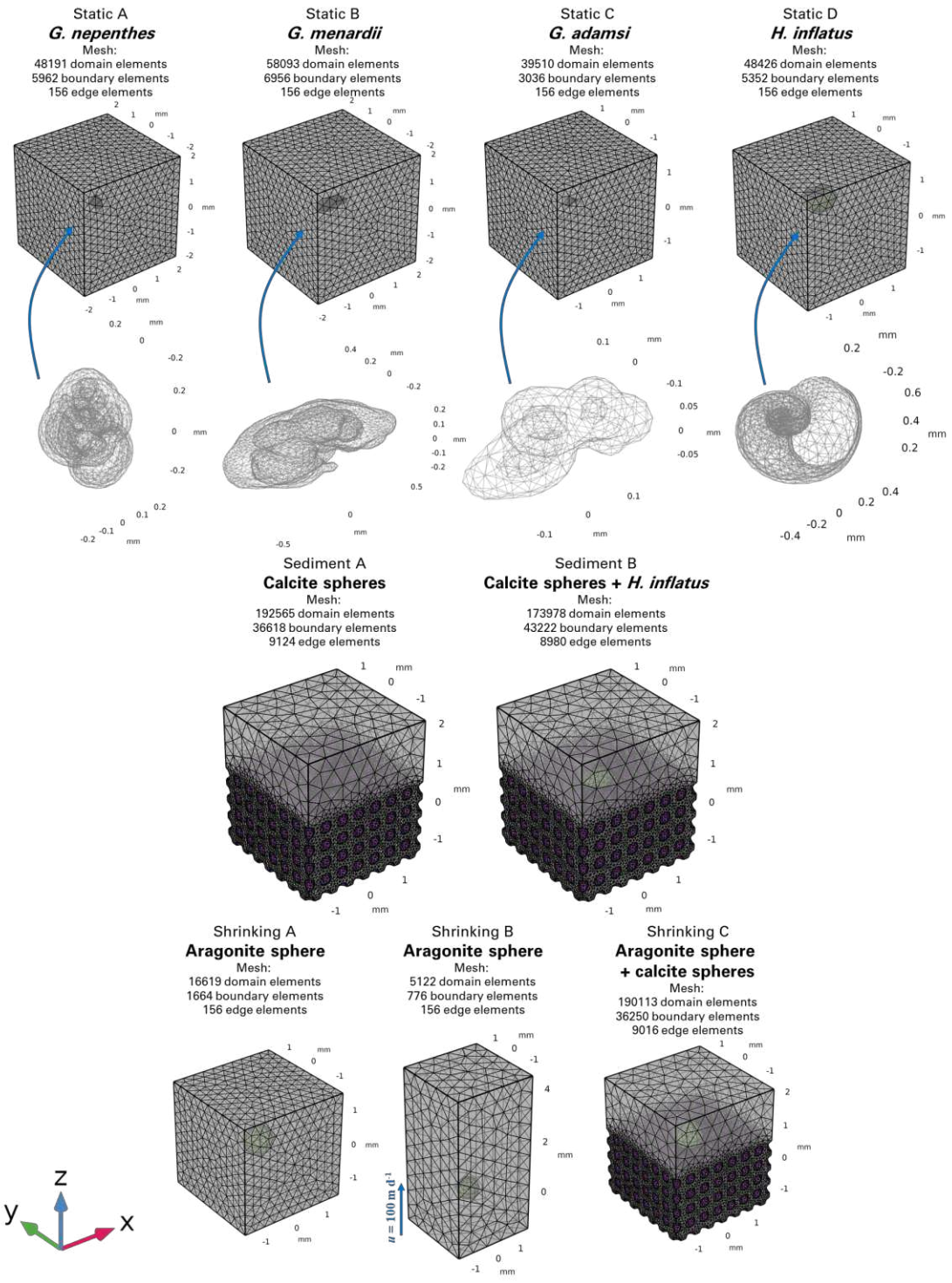

Figure S1. Summary of the different model simulations and visualization of their meshs. The top row shows the four "static" simulations in which natural $CaCO_3$ grains dissolve suspended in a volume of water. The middle row shows the two "sediment" simulations aiming to identify the role of aragonite dissolution at the seafloor on porewater chemistry and the dissolution of surrounding calcite grains. The bottom row represents the three "shrinking" simulations in which the aragonite grain mesh was reevaluated at each time step to account for the weight loss due to dissolution. Magenta color represents calcite surfaces while bright green stands for aragonite surfaces.

Table S1. Initial composition of water. Initial concentrations and total activity coefficients are from PHREEQC. Diffusion coefficients are from [a] Li and Gregory [52] and [b] Schulz [53] at 25°C.

Variable	Initial concentration (c_i, mol m^{-3})	Diffusion coefficient (D_i, m^2 s^{-1})	Total activity coefficient (γ_i, unitless)
$[H^+]$	1.166×10^{-4}	[a] 9.31×10^{-9}	0.755
$[OH^-]$	1.913×10^{-4}	[a] 5.27×10^{-9}	0.611
$[H_2CO_3^*]$	1.470×10^{-1}	[b] 1.79×10^{-9}	1.164
$[HCO_3^-]$	1.493	[a] 1.18×10^{-9}	0.676
$[CO_3^{2-}]$	3.717×10^{-3}	[a] 0.96×10^{-9}	0.209
$[Ca^+]$	10.85	[a] 0.79×10^{-9}	0.251
$[Na^+]$	497.4	[a] 1.33×10^{-9}	0.706
$[Cl^-]$	579.2	[a] 2.03×10^{-9}	0.625
$\Omega_{calcite}$	0.64		
$\Omega_{aragonite}$	0.46		
pH	7.05		

Three basic carbonate-system reactions were assumed to be instantaneous, implemented as follows:

$$H_2CO_3^* \leftrightarrow H^+ + HCO_3^- \quad \text{(R1)}, \qquad K_1 = \frac{a_{H^+}\ a_{HCO_3^-}}{a_{H_2CO_3^*}} \quad (1),$$

$$HCO_3^- \leftrightarrow H^+ + CO_3^{2-} \quad \text{(R2)}, \qquad K_2 = \frac{a_{H^+}\ a_{CO_3^{2-}}}{a_{HCO_3^-}} \quad (2),$$

$$H_2O \leftrightarrow H^+ + OH^- \quad \text{(R3)}, \qquad K_w = a_{H^+}\ a_{OH^-} \quad (3),$$

where, K_1, K_2, and K_w are equilibrium constants of the reactions at 25°C, set to $K_1 = 4.5 \times 10^{-7}$, $K_2 = 4.78 \times 10^{-11}$ [54], and $K_w = 1 \times 10^{-14}$. a_i is the activity of the i^{th} species, computed as the product of its concentration (c_i) and total activity coefficient (γ_i), the latter being obtained from PHREEQC (Table S1).

Calcite and aragonite dissolution were implemented as per:

$$\text{Calcite} \rightarrow Ca^{2+} + CO_3^{2-} \quad \text{(R4)}, \qquad K_{sp\ calcite} = a_{Ca^{2+}}\ a_{CO_3^{2-}} \quad (4),$$

$$\text{Aragonite} \rightarrow Ca^{2+} + CO_3^{2-} \quad \text{(R5)}, \qquad K_{sp\ aragonite} = a_{Ca^{2+}}\ a_{CO_3^{2-}} \quad (5),$$

where $K_{sp\ calcite}$ is the solubility constant of calcite, taken here as $10^{-8.480}$, and $K_{sp\ aragonite}$ is the solubility constant of aragonite, set at $10^{-8.336}$.[54] $CaCO_3$ reactions are not instantaneous, but instead occur with associated rates that depend on solution chemistry and on the nature of the mineral. For calcite dissolution, we use kinetics from Plummer, et al. [55], who identified three main pathways for the dissolution of calcite:

$$k_1: CaCO_3(s) + H^+(aq) = Ca^{2+}(aq) + HCO_3^-(aq) \quad (6),$$

$$k_2: CaCO_3 + H_2CO_3^* = Ca^{2+}(aq) + 2HCO_3^-(aq) \quad (7),$$

$$k_3: CaCO_3(s) = Ca^{2+}(aq) + CO_3^{2-}(aq) \quad (8).$$

The rates of these reversible reactions were combined into a single dissolution rate law:

$$R_{calcite}\ [\text{mol m}^{-2}\ \text{s}^{-1}] = (k_1\ a_{\text{H}^+} + k_2\ a_{\text{CO}_2(\text{aq})} + k_3\ a_{\text{H}_2\text{O}})\ (1 - 10^{0.67 log_{10}(\Omega_{calcite})}) \quad (9),$$

where $k_1 = 8.64 \times 10^{-5}$, $k_2 = 4.78 \times 10^{-7}$ and $k_3 = 2.34 \times 10^{-9}$ are the reaction rate constants at 25°C [56] and $a_{\text{H}_2\text{O}}$ is set to unity. Ω_{calcite} is the saturation state of water with respect to calcite defined as the ratio of the ion activity product (product of $a_{\text{Ca}^{2+}}$ and $a_{\text{CO}_3^{2-}}$) and the solubility constant of calcite. The same expression was used to compute the dissolution rate of aragonite, but Ω_{calcite} was replaced by $\Omega_{\text{aragonite}}$. This is a substantial simplification, as in reality both aragonite and calcite have specific dissolution kinetics. Nevertheless, recent laboratory experiments in seawater showed that, when normalized to the mineral surface area and for similar seawater saturation states with respect to the dissolving phase, aragonite dissolves at rates similar to calcite, if not slower[24,57]. This contrasts with earlier experiments[31] reporting very fast aragonite dissolution rates, but based on synthetic rather than biogenic aragonite and overestimated estimates of aragonite solubility[6,58]. Given that the dissolution rates derived from our model encompass measured dissolution rates at similar bulk seawater saturation states (Fig. S3), the simplified kinetic treatment applied here should be acceptable as a first approximation, and should be replaced by a more accurate mechanistic kinetic scheme developed for dissolution in seawater-type solutions when available.

To simulate the reactive-transport of each dissolved species in water, advection- diffusion-reaction equation is implemented:

$$\frac{\partial c_i}{\partial t} + \nabla \cdot (-D_i \cdot \nabla c_i) + u \cdot \nabla c_i = R_i \quad (10)$$

where, t is the time (s), ∇ is the three-dimensional space derivative operator nabla, D_i is the diffusion coefficient ($\text{m}^2\ \text{s}^{-1}$) of the i^{th} species, u is the prescribed water laminar velocity (m s^{-1}) and R_i is the reaction input ($\text{mol m}^{-3}\ \text{s}^{-1}$) of the i^{th} species.

Grains

A set of $CaCO_3$ particles was used in this study, some with shapes derived from natural grains, some more conceptual with simplified geometries; their properties are summarized in Table S2. Planktonic foraminifera shell scans of *Globoturborotalita nepenthes*, a Miocene Pacific species[59], *Globorotalia menardii*, a Pleistocene Carribean specimen[60] and *Globigerinella adamsi*, from the modern Pacific[61], were all obtained from the Tohoku University Museum *e*-foram database (http://webdb2.museum.tohoku.ac.jp/e-foram/). The *Heliconoides inflatus* pteropod shell, provided by Dr. Rosie Oakes, was obtained from a CT scan of a specimen caught at 150 m-depth in a sediment-trap located in the Cariaco Basin, in the Venezuelan shelf[62]. To make computations easier, the *H. inflatus* and *G. adamsi* e-specimens resolutions were reduced from a number of faces (triangles) of 1,969,997 and 1,107,096 for the original files, respectively, to 19,860 and 2,224 for the final geometry files imported in COMSOL. Volumes and surface areas for each grains were computed in MATLAB from the output .stl geometry files, using the Geometry and Mesh toolbox. Weights were computed by multiplying the volume of each grain by its density. The specific surface area (SSA) was computed as the surface area to mass ratio, see Table S2.

Table S2. Grain properties: species name, material, surface area, weight, specific surface area and major axis length, i.e., the widest diameter of the shell.

Name	Material	Surface area (mm^2)	Volume (mm^3)	Weight (µg)	SSA ($m^2\ g^{-1}$)	Major axis (µm)
Conceptual spheric grains						
Calcite sphere	Calcite	0.28	0.0141	37.94	0.0074	~300
Aragonite sphere	Aragonite	2.01	0.2681	785.24	0.0026	~800
Foraminifera shell scans						
G. nepenthes	Calcite	1.32	0.0226	61.25	0.0216	~620
M. menardii	Calcite	3.28	0.0839	227.37	0.0144	~1180
B. adamsi	Calcite	0.20	0.0034	9.21	0.0217	~380
Pteropod shell scans						
H. inflatus	aragonite	2.49	0.0227	66.51	0.0374	~850

Simulations

For the purposes of the present study, nine simulations were performed in total, each with different settings (Table S3). All simulation experiments and their results are made available on Zenodo (https://zenodo.org/record/5141275).

First, four dissolution simulations were performed on natural $CaCO_3$ grains kept static (i.e. in suspension) in water (Fig. S1). "Periodic" boundary conditions were applied on the external walls of water volumes, which forces concentrations on each wall to be equal to those on the opposite wall. The goal was to observe how fast each grain dissolves and what are the effects on solution chemistry within and outside the shell.

In order to quantify the effect of aragonite dissolution on porewater chemistry, two subsequent simulations were performed on $CaCO_3$ grains packed in a sediment bed (Fig. S1), one with calcite grains only and another with calcite grains and one aragonite pteropod shell. For simplicity, each calcite particle in this sediment was a sphere with a 150 µm-radius, surrogate for a typical foraminifera[63], evenly spaced so that the total porosity of this sediment is ~ 0.84, typical of a deep-sea sediment[64]. This array of calcite spheres was then placed within a 3.15 × 3.15 × 3.5 mm^3 (length × width × height, Table S3, Fig. S1) water cube, in which the bottom 1.95 mms were filled up with calcite spheres, the top 1.55 mms consisted of free water, and the sediment-water interface was located between the two. A "no flux" boundary condition was implemented at the bottom, "periodic" boundaric conditions on the sides, and on the top panel solute concentrations were fixed to their initial values.

Finally, three simulations were performed with a moving mesh, to estimate the grain size decrease due to dissolution for aragonite grains in three different environmental settings (in suspension, sinking, and in sediments, Fig. S1). To minimize computational costs, the dissolving aragonite grain in these simulations was a sphere. The simulation with the sinking grain was performed by applying a prescribed laminar water flow velocity on the z-axis of u = 100 m d^{-1}, a typical sinking speed for a pteropod[39]. Bottom and top boundary conditions were set to "no flux",

and boundary conditions on the sides were "periodic". In each simulation, a displacement rate, normal to the aragonite grain surface, was assigned to the aragonite reactive walls, computed as:

$$w_n = R_{aragonite}\, MV \quad (11)$$

where, w_n is the displacement rate defined at aragonite surface and MV is molar volume of aragonite set to 3.42×10^{-5} m^3 mol^{-1}.

Table S3. Summary of the different model simulations and their settings.

Simulation name	**Grains involved**	**Sinking speed *u*** ($m\ d^{-1}$)	**Dimensions** (mm×mm×mm) x × y × z	**Moving mesh**	**Boundary conditions**
Static A	*G. nepenthes*	0	4×4×4	No	Periodic
Static B	*G. menardii*	0	4×4×4	No	Periodic
Static C	*G. adamsi*	0	3×3×3	No	Periodic
Static D	*H. inflatus*	0	3×3×3	No	Periodic
Sediment A	Calcite spheres	0	3.15×3.15×3.5	No	Periodic, no flux, fixed
Sediment B	Calcite spheres + *H. inflatus*	0	3.15×3.15×3.5	No	Periodic, no flux, fixed
Shrinking A	Aragonite sphere	0	3×3×3	Yes	Periodic
Shrinking B	Aragonite sphere	100	3×3×6	Yes	Periodic, no flux
Shrinking C	Aragonite sphere + calcite spheres	0	3.15×3.15×3.5	Yes (for aragonite)	Periodic, no flux, fixed

Supplementary figures

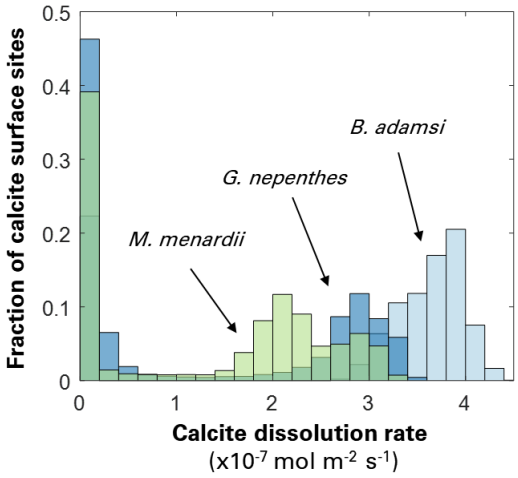

Figure S2. Bimodal distribution of foraminiferal calcite dissolution rates across the dissolving shell surface. The three foraminifera species B. adamsi (in yellow), G. nepenthes (in orange) and M. menardii (in blue) are shown in Fig. 1.

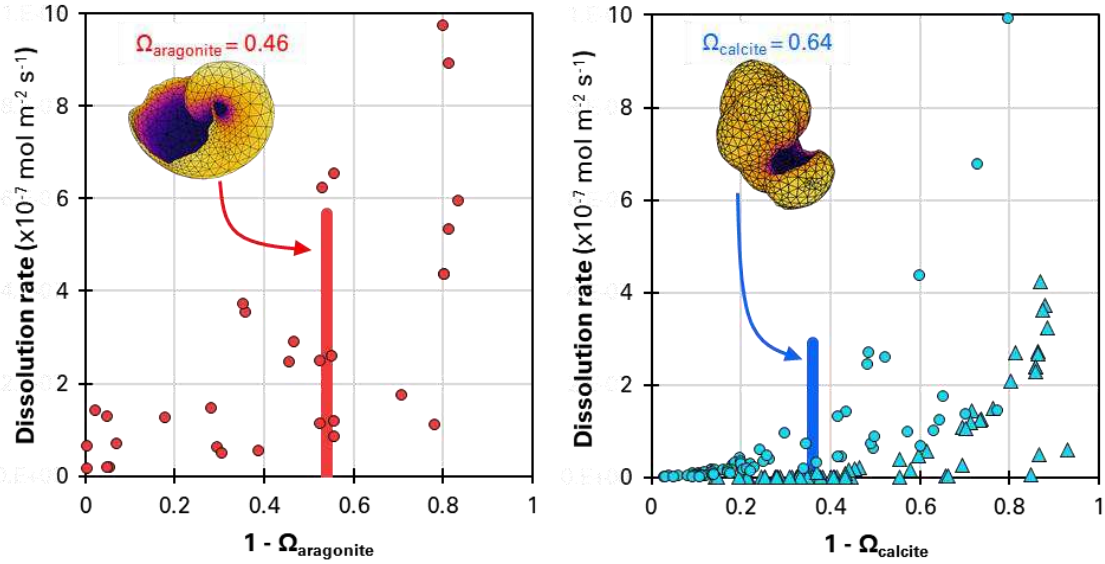

Figure S3. Steady-state grain surface area-normalized calcite (in blue) and aragonite (in red) dissolution rates as a function of the steady-state undersaturation state with respect to aragonite ($1 - \Omega_{aragonite}$) or calcite ($1 - \Omega_{calcite}$). Dots represent experimental "bulk" dissolution rates from the literature [31,33], in which the measured dissolution rates are normalized by the total area (in m^2) of the grains. Lines represent the dissolution rates as parameterized in the present study, in which the [m^{-2}] in the dissolution rate expression refers to an elementary surface area unit. Aragonite and calcite dissolution rates were recomputed using original data from Keir [31] and Walter and Morse [33]. From these two publications, all the dissolution rates from biogenic and synthetic samples were used. Units for the dissolution rates were changed to [mol m^{-2} s^{-1}] using the specific surface areas for each grain as reported in the original publications. Dissolution rates for synthetic aragonite were not reported because most of them were obtained in seawater supersaturated with respect to aragonite, thus we suspect the synthetized material was not aragonite. Saturation states were recomputed using the ionic concentration products at steady state measured by the authors, and dividing by the stoichiometric solubility constant with respect to either aragonite or calcite from Mucci [6] at the salinity and temperature of experiments, to harmonize the data.

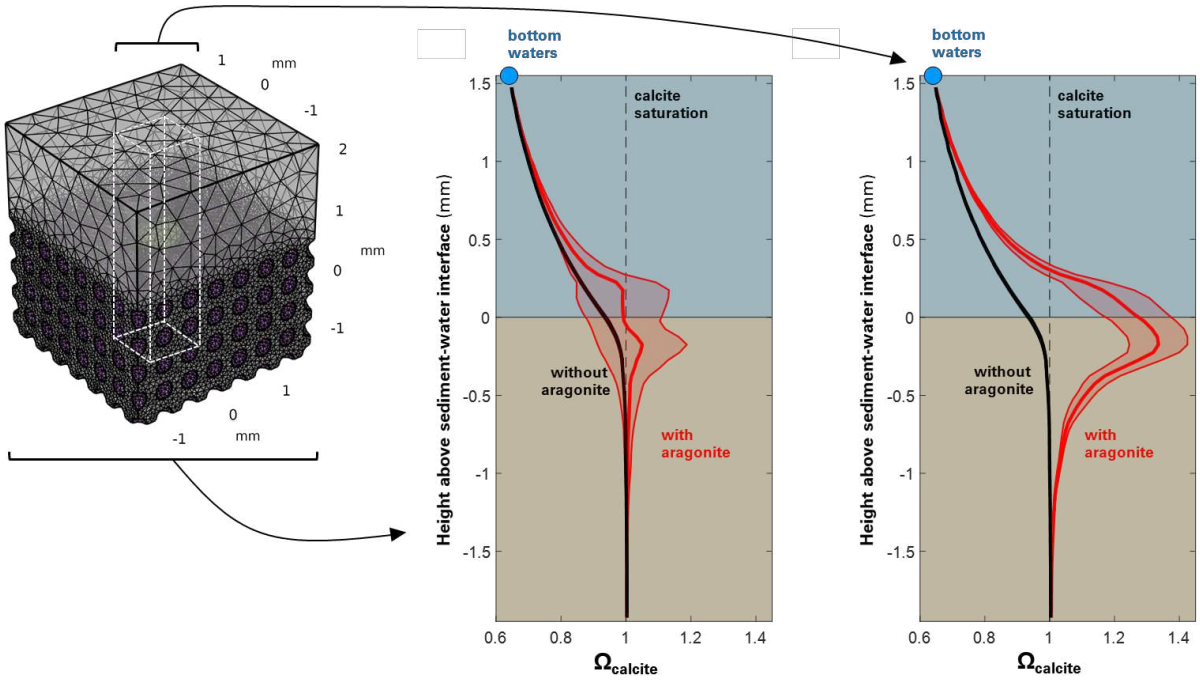

Figure S4. Depth profiles of saturation state with respect to calcite. The blue circle represents the bottom-water value, above the diffusive boundary layer. The black depth profile stands for a case without a pteropod, in which it is replaced by four calcite spheres evenly spaces one from another, while the red depth profiles represents the situation with aragonite shown on the right and in Fig. 4. The depth profile in the middle refers to the whole sediment volume whereas the depth profile on the right refers to the column just above the pteropod.

Data availability

Original foraminifera CT scans used in this study are available from the Tohoku University Museum e-foram database (http://webdb2.museum.tohoku.ac.jp/e-foram/). The pteropod CT scan is available on request to Dr. Rosie Oakes.

Code availability

All simulation experiments and their results are made available on Zenodo (https://zenodo.org/record/5141275).

Author contributions

O.S., P.A., M.W., G.M. and J.J.M. designed the research. O.S. and P.A. performed the simulations. O.S. and M.W. processed the geometry files. O.S. wrote the manuscript with contributions from all authors.

Acknowledgments

We thank Dr. Rosie Oakes at the Met Office and Dr. Osamu Sasaki at the Tohoku University Museum for providing CT scans of pteropods and foraminifera. We thank Julien Sulpis for his assistance in processing three-dimensional geometry files. O.S. and J.J.M. were supported by the Dutch Ministry of Education via the Netherlands Earth System Science Centre (NESSC). The

research work of P.A., and M.W. is part of the Industrial Partner- ship Programme i32 Computational Sciences for Energy Research that is carried out under an agreement between Shell and the Netherlands Organization for Scientific Research (NWO). M.W. has received funding from the European Research Council (ERC) under the European Union's Horizon 2020 research and innovation programme (grant agreement No. [819588]). GM is a Research Associate with the Belgian Fund for Scientific Research F.R.S-FNRS. Financial support for the work of GM was provided by the Belgian Fund for Scientific Research – F.R.S.-FNRS (project SERENATA, grant CDR J.0123.19).

Competing interests

The authors declare no conflicts of interests.

References

1 Hayes, C. T. *et al.* Global Ocean Sediment Composition and Burial Flux in the Deep Sea. *Global Biogeochemical Cycles* **35**, doi:10.1029/2020gb006769 (2021).

2 Archer, D. E. An atlas of the distribution of calcium carbonate in sediments of the deep sea. *Global Biogeochemical Cycles* **10**, 159-174, doi:10.1029/95gb03016 (1996).

3 Archer, D. *et al.* Atmospheric Lifetime of Fossil Fuel Carbon Dioxide. *Annual Review of Earth and Planetary Sciences* **37**, 117-134, doi:10.1146/annurev.earth.031208.100206 (2009).

4 Milliman, J. D. Production and accumulation of calcium carbonate in the ocean: budget of a nonsteady state. *Global Biogeochemical Cycles* **7**, 927-957 (1993).

5 Smith, S. V. & Mackenzie, F. T. The Role of $CaCO_3$ Reactions in the Contemporary Oceanic CO_2 Cycle. *Aquatic Geochemistry* **22**, 153-175, doi:10.1007/s10498-015-9282-y (2016).

6 Mucci, A. The solubility of calcite and aragonite in seawater at various salinities, temperatures and one atmosphere total pressure. *American Journal of Science* **283**, 780-799 (1983).

7 Sulpis, O., Jeansson, E., Dinauer, A., Lauvset, S. K. & Middelburg, J. J. Calcium carbonate dissolution patterns in the ocean. *Nature Geoscience* **14**, 423-428, doi:https://doi.org/10.1038/s41561-021-00743-y (2021).

8 Aumont, O., Ethé, C., Tagliabue, A., Bopp, L. & Gehlen, M. PISCES-v2: an ocean biogeochemical model for carbon and ecosystem studies. *Geoscientific Model Development* **8**, 2465-2513, doi:10.5194/gmd-8-2465-2015 (2015).

9 Moore, J. K., Lindsay, K., Doney, S. C., Long, M. C. & Misumi, K. Marine Ecosystem Dynamics and Biogeochemical Cycling in the Community Earth System Model [CESM1(BGC)]: Comparison of the 1990s with the 2090s under the RCP4.5 and RCP8.5 Scenarios. *Journal of Climate* **26**, 9291-9312, doi:10.1175/jcli-d-12-00566.1 (2013).

10 Watanabe, S. *et al.* MIROC-ESM 2010: model description and basic results of CMIP5-20c3m experiments. *Geoscientific Model Development* **4**, 845-872, doi:10.5194/gmd-4-845-2011 (2011).

11 Ilyina, T. *et al.* Global ocean biogeochemistry model HAMOCC: Model architecture and performance as component of the MPI-Earth system model in different CMIP5 experimental realizations. *Journal of Advances in Modeling Earth Systems* **5**, 287-315, doi:10.1029/2012ms000178 (2013).

12 Peijnenburg, K. *et al.* The origin and diversification of pteropods precede past perturbations in the Earth's carbon cycle. *Proc Natl Acad Sci U S A* **117**, 25609-25617, doi:10.1073/pnas.1920918117 (2020).
13 Fabry, V. J. Shell growth rates of pteropod and heteropod molluscs and aragonite production in the open ocean: Implications for the marine carbonate system. *Journal of Marine Research* **48**, 209-222 (1990).
14 Buitenhuis, E. T., Le Quéré, C., Bednaršek, N. & Schiebel, R. Large Contribution of Pteropods to Shallow CaCO3 Export. *Global Biogeochemical Cycles* **33**, 458-468, doi:10.1029/2018gb006110 (2019).
15 Bednaršek, N. *et al.* Description and quantification of pteropod shell dissolution: a sensitive bioindicator of ocean acidification. *Global Change Biology* **18**, 2378-2388, doi:10.1111/j.1365-2486.2012.02668.x (2012).
16 van Dijk, I., de Nooijer, L. J., Hart, M. B. & Reichart, G. J. The long-term impact of magnesium in seawater on foraminiferal mineralogy: Mechanism and consequences. *Global Biogeochemical Cycles* **30**, 438-446, doi:10.1002/2015gb005241 (2016).
17 Roberts, J., Wheeler, A., Freiwald, A. & Cairns, S. *Cold-Water Corals: The Biology and Geology of Deep-Sea Coral Habitats*. (Cambridge University Press, 2009).
18 Byrne, R. H., Acker, J. G., Betzer, P. R., Feely, R. A. & Cates, M. H. Water column dissolution of aragonite in the Pacific Ocean. *Nature* **312**, 321-326 (1984).
19 Oakes, R. L., Peck, V. L., Manno, C. & Bralower, T. J. Degradation of Internal Organic Matter is the Main Control on Pteropod Shell Dissolution After Death. *Global Biogeochemical Cycles* **33**, 749-760, doi:10.1029/2019gb006223 (2019).
20 Millero, F. J. Thermodynamics of the carbon dioxide system in the oceans. *Geochimica et Cosmochimica Acta* **59**, 661-677 (1995).
21 Berner, R. A. Activity coefficients of bicarbonate, carbonate and calcium ions in sea water. *Geochimica et Cosmochimica Acta* **29**, 947-965 (1965).
22 Berger, W. H. Deep-sea carbonate: pteropod distribution and the aragonite compensation depth. *Deep Sea Research* **25**, 447-452 (1978).
23 Sulpis, O. *et al.* Current $CaCO_3$ dissolution at the seafloor caused by anthropogenic CO_2. *Proceedings of the National Academy of Sciences* **115**, 11700-11705 (2018).
24 Dong, S. *et al.* Aragonite dissolution kinetics and calcite/aragonite ratios in sinking and suspended particles in the North Pacific. *Earth and Planetary Science Letters* **515**, 1-12, doi:10.1016/j.epsl.2019.03.016 (2019).
25 Adkins, J. F., Naviaux, J. D., Subhas, A. V., Dong, S. & Berelson, W. M. The Dissolution Rate of CaCO3 in the Ocean. *Ann Rev Mar Sci*, doi:10.1146/annurev-marine-041720-092514 (2020).
26 Boeuf, D. *et al.* Biological composition and microbial dynamics of sinking particulate organic matter at abyssal depths in the oligotrophic open ocean. *Proc Natl Acad Sci U S A* **116**, 11824-11832, doi:10.1073/pnas.1903080116 (2019).
27 Boudreau, B. P. A method-of-lines code for carbon and nutrient diagenesis in aquatic sediments. *Computers & Geosciences* **22**, 479-496 (1996).
28 Munhoven, G. Glacial–interglacial rain ratio changes: Implications for atmospheric and ocean–sediment interaction. *Deep Sea Research Part II: Topical Studies in Oceanography* **54**, 722-746, doi:10.1016/j.dsr2.2007.01.008 (2007).

29 Rabouille, C. & Gaillard, J.-F. Towards the EDGE: Early diagenetic global explanation. A model depicting the early diagenesis of organic matter, O_2, NO_3, Mn, and PO_4. *Geochimica et Cosmochimica Acta* **55**, 2511-2525 (1991).
30 Peterson, M. N. A. Calcite: Rates of Dissolution in a Vertical Profile in the Central Pacific. *Science* **154**, 1542-1544 (1966).
31 Keir, R. S. The dissolution kinetics of biogenic calcium carbonates in seawater. *Geochimica et Cosmochimica Acta* **44**, 241-252 (1980).
32 Subhas, A. V. *et al.* A novel determination of calcite dissolution kinetics in seawater. *Geochimica et Cosmochimica Acta* **170**, 51-68, doi:10.1016/j.gca.2015.08.011 (2015).
33 Walter, L. M. & Morse, J. W. The dissolution kinetics of shallow marine carbonates in seawater: A laboratory study. *Geochimica et Cosmochimica Acta* **49**, 1503-1513 (1985).
34 Colombani, J. The Alkaline Dissolution Rate of Calcite. *The Journal of Physical Chemistry Letters* **7**, 2376-2380, doi:10.1021/acs.jpclett.6b01055 (2016).
35 Sulpis, O., Lix, C., Mucci, A. & Boudreau, B. P. Calcite dissolution kinetics at the sediment-water interface in natural seawater. *Marine Chemistry* **195**, 70-83, doi:10.1016/j.marchem.2017.06.005 (2017).
36 Agrawal, P. *et al.* The contribution of hydrodynamic processes to calcite dissolution rates and rate spectra. *Geochimica et Cosmochimica Acta* **307**, 338-350, doi:10.1016/j.gca.2021.05.003 (2021).
37 Subhas, A. V. *et al.* The dissolution behavior of biogenic calcites in seawater and a possible role for magnesium and organic carbon. *Marine Chemistry* **205**, 100-112, doi:10.1016/j.marchem.2018.08.001 (2018).
38 Brunauer, S., Emmett, P. H. & Teller, E. Adsorption of Gases in Multimolecular Layers. *Journal of the American Chemical Society* **60**, 309-319 (1938).
39 Noji, T. T. *et al.* Clearance of picoplankton-sized partides and formation of rapidly sinking aggregates by the pteropod, *Limacina reiroversa*. *Journal of Plankton Research* **19**, 863-875 (1997).
40 Boudreau, B. P. & Guinasso, N. L., Jr. in *The Dynamic Environment of the Ocean Floor* (eds K. A. Fanning & F. T. Manheim) 115-145 (Lexington Books, 1982).
41 Boudreau, B. P., Sulpis, O. & Mucci, A. Control of CaCO3 dissolution at the deep seafloor and its consequences. *Geochimica et Cosmochimica Acta* **268**, 90-106, doi:10.1016/j.gca.2019.09.037 (2020).
42 Collen, J. D. & Burgess, C. J. Calcite Dissolution, Overgrowth and Recrystallization in the Benthic Foraminiferal Genus Notorotalia. *Journal of Paleontology* **53**, 1343-1353 (1979).
43 Pearson, P. N., Evans, S. L. & Evans, J. Effect of diagenetic recrystallization on the strength of planktonic foraminifer tests under compression. *Journal of Micropalaeontology* **34**, 59-64, doi:10.1144/jmpaleo2013-032 (2015).
44 Sun, X. & Turchyn, A. V. Significant contribution of authigenic carbonate to marine carbon burial. *Nature Geoscience* **7**, 201-204, doi:10.1038/ngeo2070 (2014).
45 Lein, A. Y. Authigenic Carbonate Formation in the Ocean. *Lithology and Mineral Resources* **39**, 1-30 (2004).
46 Gangstø, R. *et al.* Modeling the marine aragonite cycle: changes under rising carbon dioxide and its role in shallow water CaCO3 dissolution. *Biogeosciences* **5**, 1057-1072, doi:10.5194/bg-5-1057-2008 (2008).

47 Bednaršek, N., Možina, J., Vogt, M., O'Brien, C. & Tarling, G. A. The global distribution of pteropods and their contribution to carbonate and carbon biomass in the modern ocean. *Earth System Science Data* **4**, 167-186, doi:10.5194/essd-4-167-2012 (2012).
48 Emerson, S. & Bender, M. Carbon fluxes at the sediment-water interface of the deep-sea: calcium carbonate preservation. *Journal of Marine Research* **39**, 139-162 (1981).
49 Harris, R. P. Zooplankton grazing on the coccolithophore Emiliania huxleyi and its role in inorganic carbon flux. *Marine Biology* **119**, 431-439 (1994).
50 Parkhurst, D. & Appelo, C. Description of input and examples for PHREEQC Version 3—A computer program for speciation, batch-reaction, one-dimensional transport, and inverse geochemical calculations U.S. Geol. Survey Water Resources Investigations Report https://pubs.usgs.gov/tm/06/a43/ . (2013).
51 Dunne, J. P., Hales, B. & Toggweiler, J. R. Global calcite cycling constrained by sediment preservation controls. *Global Biogeochemical Cycles* **26**, GB3023, doi:10.1029/2010GB003935 (2012).
52 Li, Y.-H. & Gregory, S. Diffusion of ions in sea water and in deep-sea sediments. *Geochimica et Cosmochimica Acta* **38**, 703-714 (1974).
53 Schulz, H. D. in *Marine Geochemistry* (eds H. D. Schulz & M. Zabel) (Springer, 2006).
54 Plummer, L. N. & Busenberg, E. The solubilities of calcite, aragonite and vaterite in CO_2-H_2O solutions between 0 and 90°C, and an evaluation of the aqueous model for the system $CaCO_3$-CO_2-H_2O. *Geochimica et Cosmochimica Acta* **46**, 1011-1040 (1982).
55 Plummer, L. N., Wigley, T. M. L. & Parkhurst, D. L. The kinetics of calcite dissolution in CO_2-water systems at 5° to 60°C and 0.0 to 1.0 atm CO_2. *American Journal of Science* **278** (1978).
56 Busenberg, E. & Plummer, L. in *Studies in Diagenesis* Vol. 1578 (ed F.A. Mumpton) 139-168 (US Geological Survey Bulletin, 1986).
57 Naviaux, J. D. *et al.* Calcite dissolution rates in seawater: Lab vs. in-situ measurements and inhibition by organic matter. *Marine Chemistry* **215**, doi:10.1016/j.marchem.2019.103684 (2019).
58 Berner, R. A. Solubility of calcite and aragonite in seawater at atmospheric pressure and 34. 5% salinity. *American Journal of Science* **276** (1976).
59 Todd, R. in *Geology of Saipan, Mariana Islands. Part 3, Paleontology* Vol. 280-H (ed US Geological Survey Professional Paper) 265-320 (1957).
60 Parker, W. K., Jones, T. R. & Brady, H. B. On the nomenclature of the Foraminifera. Part X. (continued). The species enumerated by D'Orbigny in the 'Annales des Sciences Naturelles,' 1826, vol. vii. - III. The species illustrated by models. Annals and Magazine of Natural History. (3) 16 (91): 15-41. (1865).
61 Banner, F. T. & Blow, W. H. The classification and stratigraphical distribution of the Globigerinaceae. Palaeontology. 2: 1-27. (1959).
62 Oakes, R. L. & Sessa, J. A. Determining how biotic and abiotic variables affect the shell condition and parameters of <i>Heliconoides inflatus</i> pteropods from a sediment trap in the Cariaco Basin. *Biogeosciences* **17**, 1975-1990, doi:10.5194/bg-17-1975-2020 (2020).
63 Schmidt, D. N., Thierstein, H. R., Bollmann, J. & Schiebel, R. Abiotic Forcing of Plankton Evolution in the Cenozoic. *Science* **303**, 207-210 (2004).

64 Sayles, F. L., Martin, W. R., Chase, Z. & Anderson, R. F. Benthic remineralization and burial of biogenic SiO_2, $CaCO_3$, organic carbon, and detrital material in the Southern Ocean along a transect at 170 West. *Deep Sea Research II* **48**, 4323-4383 (2001).

580